

Suppressing instabilities in mixed baroclinic flow using an actuation based on receptivity

Abhishek Kumar^{1,*} and Alban Poth rat¹

Centre for Fluid and Complex Systems, Coventry University, Coventry CV1 5FB, United Kingdom

Abstract

This paper presents a method to stabilise oscillations occurring in a mixed convective flow in a nearly hemispherical cavity, using an actuation modelled on the receptivity map of the unstable mode underpinning these oscillations. This configuration represents a simplified model inspired from the continuous casting of metallic alloys where hot liquid metal is poured at the top of a hot sump with cold walls pulled in a solid phase at the bottom. The model focuses on the underlying fundamental thermo-hydrodynamic processes without dealing with the complexity inherent to the real configuration [19]. This flow exhibits three branches of instability [28]. By solving the adjoint eigenvalue problem for the convective flow equations, we find that the region of the highest receptivity for the unstable modes of each branch tends to concentrate near the inflow upper surface. Simulations of the linearised governing equations then reveal that a thermo-mechanical actuation modelled on the adjoint eigenmode suppresses the unstable mode over a finite time, after which it becomes destabilising. Based on this phenomenology, we apply the same actuation for the duration of the the stabilising phase only in the nonlinear evolution of the unstable mode. It turns out that the stabilisation persists, even when the unstable mode is left to evolve freely after the actuation period. Besides demonstrating the effectiveness of receptivity-informed actuation for the purpose of stabilising convective oscillations, these results potentially open the way to a simple strategy to control them during arbitrarily long periods of time.

1 Introduction

This paper is concerned with the suppression of oscillations in mixed convective flows in an open cavity permeated by a through-flow. It is inspired by the occurrence of such oscillations during the continuous casting of liquid metal alloys. In this type of process, solidified metal is pulled from the bottom of a pool of melted metal continuously fed from above. The pulling speed is adjusted to match that of the solidification front which, therefore, behaves as a steady but porous boundary for the fluid. A key issue is the appearance of oscillations resulting in unwanted macro-segregations [6, 15] near the axis of the melt. We previously showed that the mechanism underpinning these oscillations could be reproduced in a simple hemispherical model of the sump [19] capturing the rather unusual interplay between the baroclinic convection caused by the cooled lateral wall [47] and the through-flow [28]. Despite ignoring the complexities of the chemistry, multiple phase and solidification of the real process [30, 53, 57], the model produced three branches of linear instability: one supercritical and oscillatory, one subcritical and oscillatory, and one supercritical and non-oscillatory when the Reynolds number $Re = u_0 H / \nu$ based on the inflow velocity, sump height H and fluid kinematic viscosity ν was varied. The topology of the oscillatory modes, consistent with observations in the casting process points to their hydrodynamic nature, and so validates the simplified hydrodynamic approach. The purpose of this paper is to take further advantage of the mathematical tractability of this model to design an actuation capable of suppressing these instabilities.

The idea of suppressing oscillations by means of an actuator producing oscillations at a well-chosen location has been long-exploited in thermoacoustics [16, 31, 44], in particular to control diffusion flames in combustion [27, 34, 35]. However, it is yet to make its way to metallurgy, where oscillations occur on much larger timescales. Yet, both problems share similar challenges: The design of an effective control loop requires not only a sufficiently accurate model of the system’s dynamics but also sensors and actuators capable of feeding in the controller and enacting its output onto the process. The high temperatures, the highly corrosive nature of liquid metals and the risk of alloy contamination precludes the long term immersion of any such device in the melt. Hence, just like in combustion problems, their implementation in hostile environments often proves impractical or unreliable [41], so in both cases, open-loop control using a single actuator is preferred for its simplicity and robustness. While these techniques have long been implemented in thermoacoustics with actuators placed within the flow [32, 38], using them in liquid metals requires their positioning at the flow boundary. The key challenge is to find an actuation satisfying these conditions.

A possible solution lies in the idea of structural sensitivity, best voiced in [33]’s review on adjoint equations in stability problems: *“The key reasoning is that, if indeed a specific spatially localised region (a wave maker) acts as the driver of the oscillation and the rest of the flow just amplifies it, a structural perturbation acting in the amplifier portion is bound to affect only the amplitude (eigenvector)*

*Email: abhishek.kir@gmail.com

and not the frequency (eigenvalue) of the oscillation. Conversely, a perturbation in the wave-maker region mostly affects the eigenvalue. The structural sensitivity of the eigenvalue thus acts as a marker for the spatial location of the wave maker.” For the problem we are considering structural sensitivity thus offers a method to calculate the position and topology of the actuation best suited to suppress the growth of the unstable mode underpinning the onset of oscillations. It is all the better suited as we already identified the unstable modes in a previous linear stability analysis performed for each of the three branches appearing at different Reynolds numbers [28].

Indeed, structural sensitivity has successfully informed design alterations in devices where oscillations driven by instabilities took place, as in combustion problems or in the recent example of the stabilisation of inkjet in printers [1, 29]. The other common application of this approach concerns the *a posteriori* identification of suppression mechanisms where existing actuators are already implemented: the long misunderstood suppression of the von Kármán street by a small control cylinder placed in the near wake [54], was thus successfully explained when [37] were able to account for the feedback of the cylinder on both the unstable perturbation and the base flow. Further, a similar approach has been used in studying boundary-layer stability [9, 46]. Here we consider a slightly different approach aligned with the industrial requirements of finding actuators best suited to suppress the oscillations and adaptable when the flow parameters are varied (here the Reynolds number, for example). Since such an actuator acts either mechanically or thermally on the system, we model this combined actuation by combining an external force in the momentum equations and an external source term in the energy equation. For these to implement the alteration returned by the receptivity and sensitivity analyses, the topology and time-dependence of these source terms are matched to that of the adjoint eigenmode exactly. Doing so, however, raises two difficulties: First the linear theory does not provide an indication of the amplitude or the phase of the forcing, neither relative to that of the unstable mode, nor absolute. Both parameters therefore need to be varied to find the most effective combination for the suppression of the oscillations. Second, the system may evolve out of the linear regime where structural sensitivity operates. At this point, the system’s evolution ceases to follow that for which the forcing was designed in the first place. In control language, the system does not follow the controller’s model, so further applying the forcing may not result in the suppression predicted by the linear model. Hence the actuation may only be effective for a finite time. The question is whether this time is sufficiently long for any meaningful suppression strategy based on this approach.

We propose to answer these questions by performing the receptivity and sensitivity analyses based on the stability analysis we conducted on the mixed convective flow in a cavity in [28] and numerically apply an external forcing built as described above. Besides exploring the idea of instability suppression by sensitivity-informed external force, this problem carries three specificities of further fundamental interest from the physical and mathematical point of view: First, the mixed-convection character of this flow combines an open flow, for which structural sensitivity analysis has been perhaps most developed [21, 22, 37], with a buoyant flow, for which, to our knowledge, it was only used on stratified wakes [13]. Aside of this example, open-loop control [5, 55] and stabilisation by vibrating walls [2, 39] have been implemented in classical Rayleigh-Bénard and Marangoni flows. The adjoint equations for convective flows also made it possible to determine the influence of specific temperature distributions and heat fluxes at the flow boundaries (see [40] and others) and to infer past states of the Earth’s mantle [10, 23, 26]. Combining adjoint equations with linear stability analysis for the purpose of identifying the sources of convective instabilities and suppressing them, however, presents a new and interesting mathematical problem.

Convective flows are indeed particularly interesting in this context, as in most cases, they occur in combination with other effects such as shear flows in mixed convection (as in [59] and in the present case), or Lorentz and Coriolis forces in the vast field studying liquid planetary interiors [50]. Because of this, the path to instability may follow different branches of instability, either individually near the onset or simultaneously in more supercritical regimes, leading to multi-modality [3, 18, 24, 25, 43, 61]. For this reason, suppressing instabilities may require different actuations for different branches. These may even be used in combination in multi-modal regimes, although their effectiveness may be limited if nonlinear interactions between these modes become significant. Whether the problem of mixed convection in a cavity may become multi-modal when sufficiently supercritical is, at this point, an open question. For this reason, with in mind the aim of exploring the feasibility of suppressing convective oscillations using sensitivity-informed actuation, we shall restrict ourselves to weakly supercritical regimes where instabilities are driven by a single unstable mode in each of the three branches of instability. This still leaves the question open as to whether the approach would be equally effective for each of them, especially so as these occur through bifurcations of different nature. Hence, we shall seek answers to the following questions:

- (i) Does the system have significant receptivity in regions of the flow where an actuation can realistically be applied, in particular near the boundaries?
- (ii) Which forcing parameters (phase and amplitude) are best suited to apply an external thermo-mechanical actuation modelled on the adjoint to the eigenmode to suppress?
- (iii) By how much can the energy of the oscillations be reduced and for how long?
- (iv) Does an actuation purely based on linear dynamics remain effective when the nonlinearities are accounted for?

To answer these questions, we start by formulating the adjoint problem for mixed baroclinic convection in a nearly-hemispherical cavity, as defined by [28] and recalled in § 2, along with a description of the numerical system based on high-order spectral elements methods. We then identify the thermo-mechanical source of the instabilities by performing receptivity and sensitivity analyses (§ 3). To determine the optimal phase and amplitude of the actuation based on the adjoint mode, relative to the unstable mode, we evolve the linearised equations, varying these values (§ 4). Finally, we put the idea to the test in fully nonlinear simulations and assess how long nonlinearities are kept at bay (§ 5).

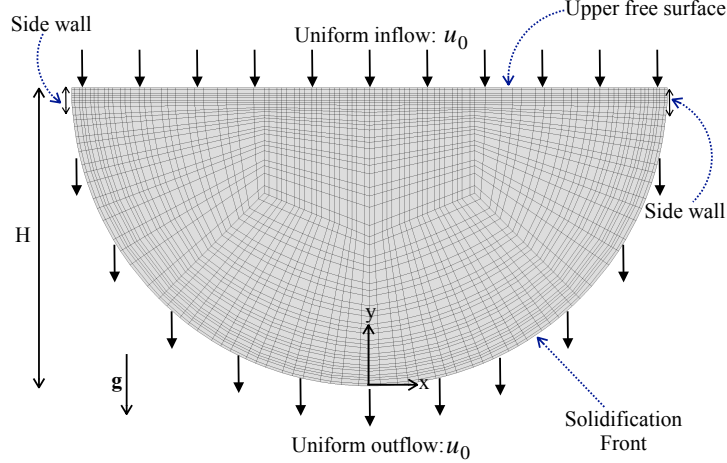


Figure 1: Problem geometry and mesh, with a rigid free surface at the inlet (top), solid side walls, and a porous solid wall at the outlet (bottom, solidification front). The flow enters and leaves the domains at vertical velocity u_0 . The sketch also shows details of the mesh. This mesh consists of 348 quadrilateral elements, and each element is represented by the polynomial order of $N = 3$. Thus, the total collocation points are $348 \times (N + 1)^2 = 5568$.

2 Problem formulation

2.1 Governing equations

Following [28], we consider a cavity of height H with an upper free surface where hot fluid is fed in, and a cold, porous lower boundary representing a solidification front, as shown in figure 1. The cavity is also assumed infinitely extended in the third direction (\mathbf{e}_z). The lower boundary is semicircular and connected to the flat upper boundary by two solid, adiabatic side walls of height $0.05H$, with a temperature difference ΔT between top and bottom boundaries. To model a liquid metal of density ρ , kinematic viscosity ν , thermal diffusivity α , thermal expansion coefficient β , the flow is assumed Newtonian and since temperature gradients remain moderate, its motion is assumed well described by the Oberbeck–Boussinesq approximation [8, 12, 45]. This leads to the following non-dimensional governing equations:

$$\frac{\partial \mathbf{u}}{\partial t} + (\mathbf{u} \cdot \nabla) \mathbf{u} + \nabla p = Ra Pr T \mathbf{e}_y + Pr \nabla^2 \mathbf{u}, \quad (1)$$

$$\frac{\partial T}{\partial t} + (\mathbf{u} \cdot \nabla) T = \nabla^2 T, \quad (2)$$

$$\nabla \cdot \mathbf{u} = 0, \quad (3)$$

where $\mathbf{u} = (u, v, w)$ is the velocity vector field, T is the temperature field, t is the time, and $\mathbf{g} = -g\mathbf{e}_y$ is the gravitational acceleration. The modified pressure p includes the buoyancy term that accounts for the reference temperature T_0 at density ρ_0 [12, 58]. The above set of equations are non-dimensionalised using length H , velocity α/H , time H^2/α , pressure $\rho_0(\alpha/H)^2$ and temperature ΔT . The equations feature two governing non-dimensional groups: The Prandtl number

$$Pr = \frac{\nu}{\alpha}, \quad (4)$$

which we fixed to 0.02, a typical value of aluminium alloys, and the Rayleigh number Ra , defined as

$$Ra = \frac{\beta g \Delta T H^3}{\nu \alpha}, \quad (5)$$

which controls the intensity of buoyancy forces relative to viscous forces. A free-slip boundary condition is applied to the upper boundary at $y = 1$ with fluid being poured homogeneously across the boundary at an imposed temperature ΔT . These boundary conditions are expressed as:

$$\frac{\partial}{\partial y} \mathbf{u} \times \mathbf{e}_y = 0, \quad \mathbf{u} \cdot \mathbf{e}_y = Re Pr, \quad T(y = 1) = 1, \quad (6)$$

where Re is the mass flux Reynolds number based on the dimensional feeding velocity u_0

$$Re = \frac{u_0 H}{\nu}. \quad (7)$$

At the lower boundary \mathcal{S} , the solidification front is represented by solid, porous boundary conditions:

$$\mathbf{u}_S \times \mathbf{e}_y = 0, \quad \mathbf{u}_S \cdot \mathbf{e}_y = RePr, \quad T_S = 0, \quad (8)$$

such that the flux of fluid pulled at \mathcal{S} exactly cancels the flux of mass coming from the inlet. Impermeable, no-slip boundary conditions for the velocity field and insulating boundary conditions for the temperature field are imposed at the side-walls (see figure 1). These boundary conditions for the temperature field at these side-walls ensure that the temperature field remains continuous along the entire periphery of the domain. In the third direction \mathbf{e}_z , the domain's infinite extension is represented by periodic boundary conditions for all flow fields.

2.2 Direct and adjoint perturbation equations

The purpose of this work is to suppress linear instabilities with an actuation specifically designed to stifle the growth of linear perturbations. Since this actuation will be based on the linear dynamics of this perturbation, we first need to establish the set of equations that govern its linear dynamics. From [28], linear perturbations grow from a class of equilibrium solutions of Eqs. (1-3) and boundary conditions (6, 8) that are planar and invariant along \mathbf{e}_z , hence of the form $\mathbf{U}(x, y), \bar{T}(x, y)$. Baroclinicity due to the isothermal condition along the solidification front precludes any purely diffusive thermal equilibrium, so $\mathbf{U}(x, y)$ is never homogeneously zero and both $\mathbf{U}(x, y)$ and $\bar{T}(x, y)$ must be found as a fully nonlinear two-dimensional solution of the equations. It follows that perturbations to this equilibrium $\mathbf{q}'(x, y, z, t) = (\mathbf{u}, T)^\top - (\mathbf{U}, \bar{T})^\top = (\mathbf{u}'(x, y, z, t), T'(x, y, z, t))^\top$, are governed by the linear system of equations governing the evolution of infinitesimal perturbations,

$$\frac{\partial \mathbf{q}'}{\partial t} = \mathcal{L} \mathbf{q}', \quad (9)$$

where

$$\mathcal{L} \mathbf{q}' = \begin{pmatrix} -(\mathbf{U} \cdot \nabla) \mathbf{u}' - (\nabla \mathbf{U}) \cdot \mathbf{u}' - \nabla p' + RaPrT' \mathbf{e}_y + Pr \nabla^2 \mathbf{u}' \\ -\mathbf{U} \cdot \nabla T' - (\nabla \bar{T}) \cdot \mathbf{u}' + \nabla^2 T' \end{pmatrix} \quad (10)$$

and p' is determined by the constraint $\nabla \cdot \mathbf{u}' = 0$. We will refer to equation (9) as the direct perturbation equation, and to \mathcal{L} as the direct linear operator. The boundary conditions for the base flow are the same as those for the main variables. As a result, the perturbation variables satisfy the homogeneous counterparts of the boundary conditions associated with the base flow. Since the base flow is invariant along \mathbf{e}_z and \mathcal{L} does not explicitly depend upon time, the perturbation can be written as a linear combination of normal modes of the form:

$$\mathbf{q}'(x, y, z, t) = \hat{\mathbf{q}}(x, y) e^{ikz + \lambda t}, \quad (11)$$

where k is the wavenumber along the homogenous direction \mathbf{e}_z and $\lambda = \sigma \pm i\omega$ contains the growth rate, σ and frequency ω . The growth rate, frequency, and the wavenumber of the most dominant mode $\hat{\mathbf{q}}(x, y) = (\hat{u}, \hat{v}, \hat{w}, \hat{T})^\top$ (also referred to as the direct mode) are found by solving the eigenvalue problem for λ that result from (9) and (11). This is done numerically by means of a time-stepper method [4]. Here the eigenmodes are normalised such that $\|\hat{\mathbf{q}}\|_2 = 1$, where $\|\cdot\|_2$ denotes the standard l^2 vector norm of $4 \times N_e \times (N + 1)^2$ values that make up $\hat{\mathbf{q}}$. In this context, N_e refers to the number of quadrilateral elements. For the details of the eigenvalue solver we refer the reader to section 2.2 of our previous work [28].

Next, we need to work out the form of the actuation that is best suited to suppress the growth of individual normal modes. The idea we pursue relies on [22]'s ideas, who showed that the receptive regions of the direct linear modes are mapped by the adjoint eigenmodes of the same linearised equations. We, therefore, need to construct the adjoint operator \mathcal{L}^* with respect to the time-averaged inner product relevant to the problem [36]:

$$(\mathbf{a}, \mathbf{b}) = \int_{\Omega} \mathbf{a} \cdot \mathbf{b} dV, \quad \langle \mathbf{c}, \mathbf{d} \rangle = \int_0^\tau (\mathbf{c}, \mathbf{d}) dt, \quad (12)$$

where \mathbf{a} and \mathbf{b} are time-averaged vector fields defined on the fluid domain Ω , while \mathbf{c} and \mathbf{d} are time-dependent vector fields defined on Ω and time domain $[0, \tau]$. The adjoint operator is then defined by the relation

$$\langle \mathbf{q}^*, (-\partial_t + \mathcal{L}) \mathbf{q}' \rangle - \langle (\partial_t + \mathcal{L}^*) \mathbf{q}^*, \mathbf{q}' \rangle = 0, \quad (13)$$

and thus satisfies:

$$-\frac{\partial \mathbf{q}^*}{\partial t} = \mathcal{L}^* \mathbf{q}^*, \quad (14)$$

where $\mathbf{q}^*(x, y, z, t) = (u^*, v^*, w^*, T^*)^\top$ represents adjoint variables. The expression of \mathcal{L}^* is readily derived from the direct perturbation equation (9) by integration by parts:

$$\mathcal{L}^* \mathbf{q}^* = \begin{pmatrix} (\mathbf{U} \cdot \nabla) \mathbf{u}^* - (\nabla \mathbf{U})^\top \cdot \mathbf{u}^* - (\nabla \bar{T}) T^* - \nabla p^* + Pr \nabla^2 \mathbf{u}^* \\ (\mathbf{U} \cdot \nabla) T^* + RaPr v^* + \nabla^2 T^* \end{pmatrix} \quad (15)$$

with $\nabla \cdot \mathbf{u}^* = 0$. Similarly, the adjoint variables satisfy adjoint boundary conditions imposed by equation (13). These are identical to the boundary conditions satisfied by the direct variables, except for the \mathbf{e}_x and \mathbf{e}_z components of the velocity field at the upper free surface, that must satisfy Robin conditions [4]:

$$\mathbf{e}_y \cdot \nabla u^* - Re u^* = 0; \quad \mathbf{e}_y \cdot \nabla w^* - Re w^* = 0. \quad (16)$$

Like the direct variables, the adjoint variables are decomposed into the normal modes but obtained as the solution of the adjoint eigenvalue problem, instead of the direct one so this time, the same eigenvalue solver yields the adjoint mode $\hat{\mathbf{q}}^*(x, y) = (\hat{u}^*, \hat{v}^*, \hat{w}^*, \hat{T}^*)^\top$. It follows from the bi-orthogonality property that the growth rate and the frequency of the adjoint and direct modes are identical [51].

2.3 Receptivity and sensitivity

[22] showed that the adjoint field represented Green's function for the receptivity problem. Therefore, the adjoint equations can be used to evaluate the effects of any external forcing to the solution of equation (9). This property forms the basis for the analysis in § 4, where we seek to identify the regions where applying an actuation would most effectively affect the growth of unstable modes. To assess this, we use the property that the relative shift in the eigenvalue, and therefore the growth rate associated to the direct and the adjoint mode incurred by acting at any given location of the flow is given by the sensitivity tensor [21, 22, 49]

$$S_{ij}(x, y) = \frac{\hat{\mathbf{q}}_i \hat{\mathbf{q}}_j^*}{\int_{\Omega} \hat{\mathbf{q}} \cdot \hat{\mathbf{q}}^* dx dy}. \quad (17)$$

This tensor determines the relative local intensity of the feedback of individual component $\hat{\mathbf{q}}_j^*$ onto the individual component $\hat{\mathbf{q}}_i$ of the eigenmode. In particular, since \mathbf{q}' and \mathbf{q}^* contain all three components of velocity and the temperature, the knowledge of S_{ij} indicates whether the actuation should be of thermal or mechanical nature and if mechanical, which component of the velocity (or combination of all four components including temperature) is most efficient at altering the growth of the unstable mode. Both the direct and adjoint problems being linear, amplitudes are relative so we may further normalise the direct and adjoint modes by choosing [22]:

$$\int_{\Omega} \hat{\mathbf{q}} \cdot \hat{\mathbf{q}}^* dx dy = 1, \quad (18)$$

so that the sensitivity tensor is simply expressed as $S_{ij} = \hat{\mathbf{q}}_i \hat{\mathbf{q}}_j^*$.

2.4 Methodology and choice of parameters

For the remainder of the paper, we shall proceed as follows to find and assess the actuation best suited to damp the growth of linear instabilities: First, the steady base two-dimensional solutions are obtained using direct numerical simulation (DNS) of (1)-(3) together with the associated boundary conditions. Second, the linear stability analysis (LSA) of the two-dimensional base flow against three-dimensional perturbations is carried out by solving the eigenvalue problem for operator \mathcal{L} . These first two steps were previously carried out over an extensive range of governing parameters and wavenumbers k in [28]. Here, we repeat the same approach for flows that are weakly supercritical so as to focus on cases where the instability is driven by a small number of unstable modes. The idea behind this strategy is that even in the fully nonlinear evolution, if the instability remains driven by a small enough number of modes, it may be enough to prevent the growth of the most unstable of them to stop the growth of instabilities altogether. This approach is not expected to be successful if the base flow is destabilised by a broad spectrum of fast growing unstable modes, as may be the case in more strongly supercritical cases. On this basis, we select four typical weakly supercritical cases illustrating the different instability mechanisms identified in this previous work.

- C1 ($Re = 0; Ra = 7 \times 10^3$): This case corresponds to a purely convective base flow with zero inlet (and outlet) mass flux, *i.e.*, no fluid crosses the boundaries of the flow domain (see figure 2(a)). The flow becomes unstable to a travelling wave at $Ra_c = 5.975 \times 10^3$, through a supercritical Hopf bifurcation. The corresponding branch in the complex eigenmode spectrum is labelled type II.
- C2 ($Re = 50; Ra = 7 \times 10^3$): This case features an inflow through the upper boundary as shown in figure 2(b). The flow becomes unstable to a type II travelling wave through a supercritical Hopf bifurcation.
- C3 ($Re = 100; Ra = 4 \times 10^4$): This case is similar to C2 but with more intense inflow. The base flow is presented in figure 2(c). At $Ra_c = 3.621 \times 10^4$, it becomes unstable to a leading mode from a different branch (type I), that is still oscillatory but arises out of a subcritical Hopf bifurcation.
- C4 ($Re = 150; Ra = 8 \times 10^4$): Here the flow is mostly driven by the inflow (see figure 2(d)). The instability corresponds to a further branch of the eigenvalue spectrum labelled type III and yields a non-oscillatory mode through a supercritical pitchfork bifurcation.

Simulation Case	Re	Ra	$(Ra/Ra_c) - 1$	N_U	k
C1	0	7×10^3	0.17	2	6
C2	50	7×10^3	0.13	2	6
C3	100	4×10^4	0.10	1	4
C4	150	8×10^4	0.09	1	6

Table 1: Parameters of the weakly supercritical cases, C1, C2, C3, and C4, were selected for the analysis. Here $(Ra/Ra_c) - 1$ represents the level of criticality, where Ra_c is the critical Rayleigh number, N_U represents the number of unstable modes, and k represents the most unstable mode. Note that Ra_c for the each case is obtained from the table 2 of [28].

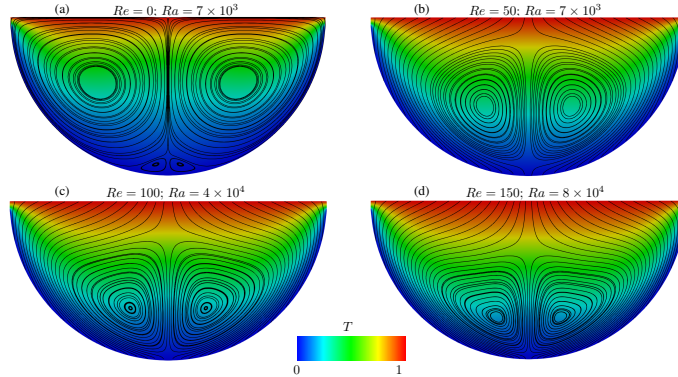


Figure 2: Streamlines of the steady two-dimensional base flow and temperature field for the simulation cases (a) C1, (b) C2, (c) C3, and (d) C4.

Details of the above selected parameters are tabulated in table 1.

Additionally to this previous analysis, we now need to calculate adjoint modes to perform the receptivity and sensitivity analyses (RSA). These are obtained by solving the eigenvalue problem for the operator \mathcal{L}^* using the same method as for the LSA. Third, the evolution of the normal mode targeted for suppression is calculated using the linearised Navier–Stokes equations (9), to which a forcing term based on the adjoint eigenmode is added on the left hand side. This forcing term is defined as follows:

$$\mathbf{f}(x, y, z, t) = \Re\{A\hat{\mathbf{q}}^*(x, y) \exp[\sigma t + i(kz + \omega t + \phi)]\}, \quad (19)$$

where A and ϕ represents the real amplitude and real phase of the forcing, respectively, relative to the unstable mode. Force \mathbf{f} has four components. The first three components represent mechanical forces, and the last component represents thermal forces. This step serves two purposes. First, it acts as a validation of the strategy. Since the forcing is derived from linearised adjoint equations, that ignore nonlinear interactions, it must at least be effective at damping the direct linear mode, to carry any hope of preventing the full nonlinear growth of the instability. Second, building the forcing on the topology of the adjoint mode involves a choice of amplitude and phase relative to the direct modes. To find out the optimal values of both, we carry out a series of linear simulations where they are varied.

Finally, with the knowledge of the optimal amplitude and phase of the actuation, we test the suppression of instability with its full nonlinear dynamics through three-dimensional (3D) DNS (the detail of individual simulations are given in § 5).

2.5 Numerical set-up

The methodology outlined in the previous section involves four types of numerical computations: 2D (nonlinear) DNS, direct and adjoint eigenvalue problems, 3D evolution of individual eigenmodes through the direct linearised equations and 3D (nonlinear) DNS. The solution of the direct and adjoint eigenvalue problems are found by means of the time-stepping method implemented and tested in detail in [28]. The novelty compared to this previous work is the solution of the adjoint eigenvalue problem, which was validated by making sure the eigenvalues obtained from both the LSA and RSA yielded the same results down to machine precision.

The non-linear governing equations (1)-(3), the direct perturbation equation (9), and the adjoint equation (14) are solved using the spectral-element code Nektar++ [11, 42]. We adopted a spectral-element discretisation in the $x - y$ plane with a mesh consisting of 348 quadrilateral elements. For the three-dimensional simulations, we used a Fourier-based spectral method [7] for discretisation in the e_z direction. The computational domain extends along e_z by 2π . A third-order implicit-explicit (IMEX) method [60] is used for time-stepping. For all four types of numerical calculations, the time step was kept constant so that the maximum local Courant number

N	σ	Relative error (%)
6	0.21598	1.67593
7	0.21293	0.24009
8	0.21249	0.03295
9	0.21242	—

Table 2: We examine the relationship between the leading eigenvalues and the polynomial order N . The leading eigenvalues are computed on the mesh at $Re = 150$, $Ra = 8 \times 10^4$, and $k = 6$. The relative error is calculated with respect to the case of the highest polynomial order ($N = 9$).

C_{\max} remained below unity everywhere in the domain at all times. Table 4 lists the values of time step Δt for each set of simulations. The numerical implementation is described and tested in detail in [28]. Figure 1 shows the details of a two-dimensional $x - y$ mesh generated using the GMSH package [20] with polynomial order $N = 3$ as an example of spatial-spectral discretisation used in the (x, y) plane. Elements at the edges are more densely packed than in the bulk, with a ratio of four between the edge sizes of the largest and the smallest elements. On each element, the flow variables are projected onto the polynomial basis represented at Gauss–Lobatto–Legendre points. As in our previous work, we perform a convergence test on the polynomial order for the leading eigenvalue for each case to ensure the solution is independent of the spectral order. For example, the leading eigenvalue computed for the simulation case C4 with the polynomial order $N = 8$ differs by less than 0.04% from the calculation performed with $N = 9$. Convergence of the leading eigenvalue with the polynomial order is presented in table 2. Similar convergence tests have been conducted for other simulation cases. The order of polynomials retained for each case is listed in table 4. For all 3D DNS calculations, we have retained 32 Fourier modes along e_z , which are deemed adequate based on our previous convergence test conducted in [28].

3 Linear receptivity and sensitivity analyses

The aim of this section is to identify the most effective location within the flow domain for an actuation to suppress instabilities using RSA. The receptivity analysis returns a map of the physical locations within the flow domain where one can act on the instabilities by applying an external actuation. On the other hand, the sensitivity analysis identifies the location in the flow domain where this external actuation would incur the greatest flow alteration. For this purpose, we shall discuss each of the cases C1–C4 outlined in § 2.4.

3.1 Sensitivity and receptivity maps

For C1, the base flow, represented on figure 2(a), consists of two symmetric baroclinically-driven recirculation cells driven along the solidification front, from the maximum baroclinicity regions in the upper left and right corners. Both cells meet on the axis near the bottom of the domain and drive a strong upward jet there. The leading unstable mode of type II (with critical parameters $k_c = 6.3$, $Ra_c = 5.975 \times 10^3$) arises out of shear instability near the location of the maximum velocity along that jet (see figure 3(a)). It consists of a wave travelling in the z direction, and appears through a supercritical Hopf bifurcation.

The velocity field modulus associated to the adjoint mode $\|\hat{u}^*\|$, which represents receptivity, is displayed in figure 3(b). The most receptive region is located at the wall, where the magnitude of two jets is strongest. The product of direct and adjoint modes represents the sensitivity and is plotted in figure 3(c). This plot shows that the sensitivity is symmetric about the central axis, and strong towards the bottom of the cavity. This topology does not overlap very well with the location of the instability. This implies that acting on the region of high sensitivity would not necessarily directly impact the development of the instability in this case.

For C2, the presence of the inflow through the top boundary opposes the upward jet seen in C1 and therefore suppresses the baroclinically-driven recirculation. These are displaced downwards as a result and the shear is less concentrated near the symmetry axis as represented in figure 2(b). Accordingly, the unstable mode ($k_c = 6.2$, $Ra_c = 6.168 \times 10^3$, figure 3(d)) is more widely spread along the two directions of space than in C1 and stretches down to the bottom of the cavity. It also separates into two lobes corresponding to each recirculation, whilst keeping a maximum intensity where they meet at the bottom of the cell. The most receptive region (see figure 3(e)) lies just below the upper surface, where the fluid flows into the cavity from either side of the central axis. The sensitivity, as shown in figure 3(f), is particularly strong at the bottom of the domain, where oscillations are caused by the instability. The topology of the receptive mode has two consequences: First, the most effective location to act on instability is not in the bulk of the flow, but near the top surface. Since the inflow directly impacts this region, altering the inflow profile may offer an effective means of applying optimal actuation. Second, if we apply an actuation built from the topology of the receptivity map, then its maximum effect will be located near the bottom of the cavity, precisely where the LSA identified the instability’s origin. Therefore, such an actuation would likely effectively influence the development of the instability.

In case C3, the greater inflow compared to C2 further suppresses the convective cells. These now become confined to the lower half of the domain, and extend over less than a third of its width (see figure 2(c)). The topology of the unstable mode ($k_c = 4.1$, $Ra_c = 3.621 \times 10^4$, figure 3(g)) remains similar to that of C2, but the lobes of greater energy are now separated along the jet to join

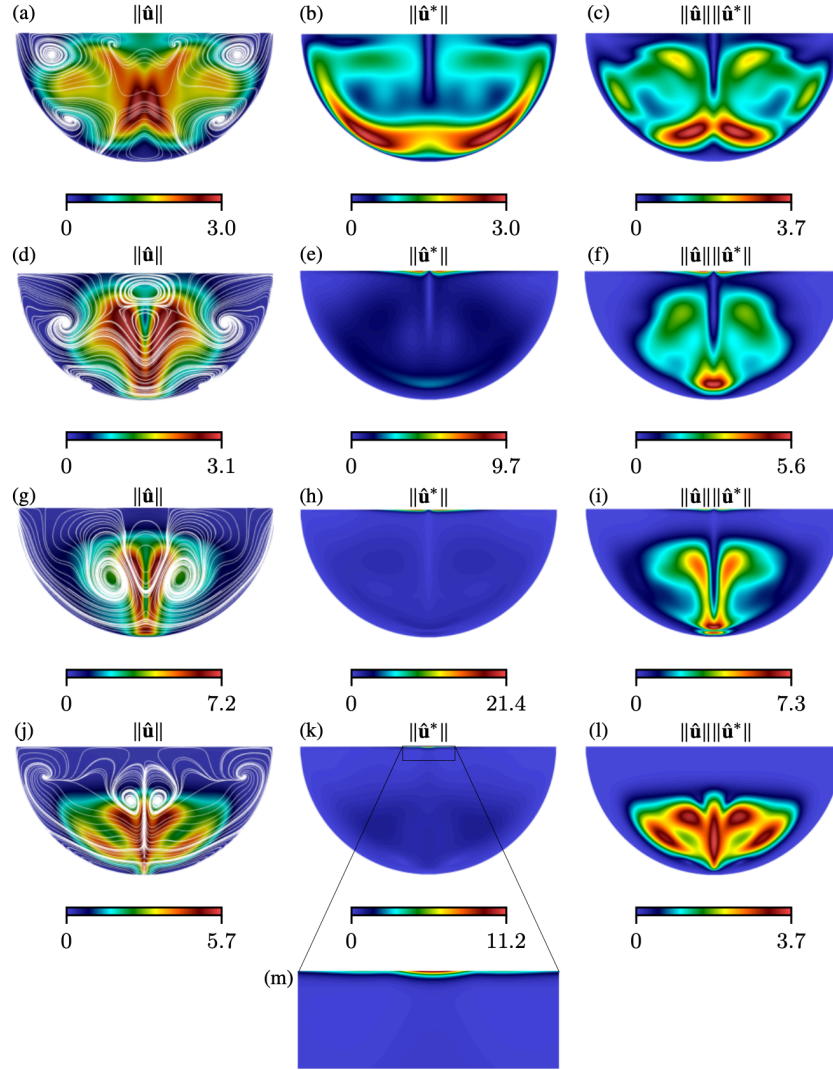


Figure 3: Spatial distribution of the velocity field modulus ($\|\hat{\mathbf{u}}\|$), receptivity to momentum forcing ($\|\hat{\mathbf{u}}^*\|$), and the Frobenius norm of the momentum structural sensitivity ($\|\hat{\mathbf{u}}\|\|\hat{\mathbf{u}}^*\|$) for the simulation cases: (a)-(c) C1; (d)-(f) C2; (g)-(i) C3; (j)-(l) C4. (m) Represents the zoomed region of $\|\hat{\mathbf{u}}^*\|$ for C4. The streamlines in (a), (d), (g), and (j) represent the real part of the unstable eigenmode ($\Re(\hat{u})\mathbf{e}_x + \Re(\hat{v})\mathbf{e}_y$) in the $x - y$ plane.

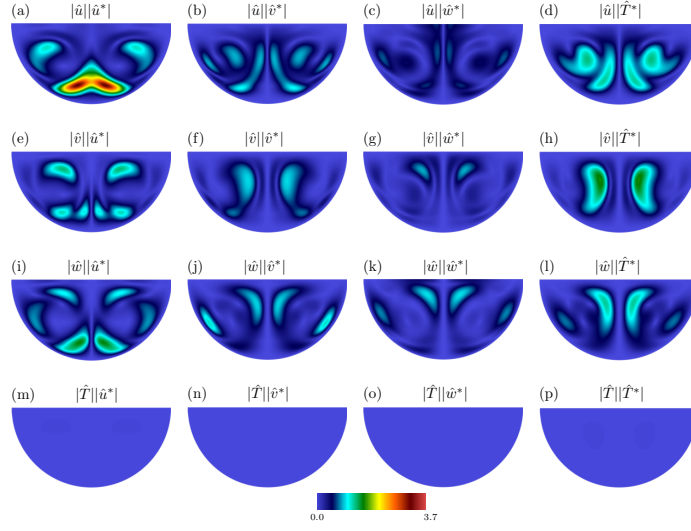


Figure 4: The absolute value of the components of the sensitivity tensor $S_{ij} = \hat{\mathbf{q}}_i \hat{\mathbf{q}}_j^*$ for the simulation case C1 ($Re = 0$, $Ra = 7 \times 10^3$, and $k = 6$) in the $x - y$ plane.

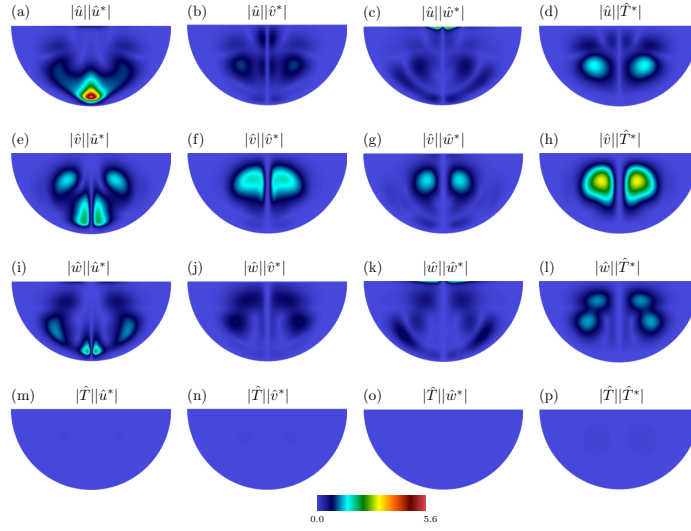


Figure 5: The absolute value of the components of the sensitivity tensor $S_{ij} = \hat{\mathbf{q}}_i \hat{\mathbf{q}}_j^*$ for the simulation case C2 ($Re = 50$, $Ra = 7 \times 10^3$, and $k = 6$) in the $x - y$ plane.

only near the bottom where the mode's energy is still maximum. The receptivity is again concentrated near the top surface but has further contracted in size (see figure 3(h)). Here the topology of the sensitivity (figure 3(i)) follows that of the unstable mode practically everywhere in the domain, not just near their maxima. This suggests that the effect of an actuation shaped on the receptivity mode may affect the unstable mode not only in its region of maximum intensity but also over the entire spatial extension.

Lastly, case C4 corresponds to a different regime where the inflow further suppresses the convective cells (see figure 2(d)). The unstable mode ($k_c = 6.0$, $Ra_c = 7.345 \times 10^4$, figure 3(j)) adopts a different topology with a sharp maximum along the central axis and four lobes extending either side of it in the middle of the bulk and near the bottom wall. These correspond to the location where streamlines are at maximum angle with the vertical direction. Somewhat surprisingly, despite a very different topology in their leading eigenmode, the receptivity modes in C3 and C4 exhibit relatively similar topologies, both of them being sharply concentrated in the middle of the free surface. The receptive mode of C4, however, is concentrated over an even smaller region (see figure 3(k)). Additionally, in contrast to C2 and C3, the receptivity mode for C4 features a maximum exactly in the middle of the inlet, visible on magnified figure 3(m) whereas the receptivity modes for C2 and C3 are split into two lobes, each with a point of maximum intensity either side of the centre of the free surface.

3.2 Sensitivity tensor

We now examine the sensitivity tensor S_{ij} to determine how individual components of the temperature and velocity fields respond to actuation on each of their components, as discussed in § 2.3.

The first noticeable feature is that in all four cases C1–C4 represented on figures 4 to 7, all elements of the tensor associated to $|\hat{T}|$, are practically identically zero, including $|\hat{T}||\hat{T}^*|$. This means that the temperature perturbation responds to no actuation, not even a thermal one. On the other hand components of the tensor involving a velocity component and $|\hat{T}^*|$ all show a strong response, so that the temperature field of the perturbation can likely be affected by a mechanical actuation. This can be understood in view of the low value of Pr considered here (and for other liquid metals): even if a given actuation overcomes viscous forces to acts on the velocity field, it would still need to act on a $\mathcal{O}(Pr)$ timescale to overcome thermal diffusion and affect the temperature field. Consequently, at low Pr , the instability is better acted upon through its velocity field, *i.e.*, mechanically.

In case C1, figure 4(a) highlights that the greatest feedback is received by x -component of the velocity from the perturbation, from the x -velocity component of the actuation. The maximum coincides with the lower part of the flow domain where the baroclinic jets turns up, just upstream of the point where they meet each other, and where the instability starts. C2 also features maximum feedback from \hat{u}_x^* onto \hat{u}_x . This time, however, the sensitivity area is localised right at the bottom of the domain, at the point where the instability is maximum in velocity amplitude. Cases C3 and C4 by contrast, exhibit the greatest response to a temperature actuation. All three components show high response in both cases. In C3, the maximum receptivity is on the v component, but on the u component for C4.

4 Linear response to an actuation based on receptivity modes

Having now identified the topology of the receptivity modes and their likely effect on the instability, we shall now proceed to use these modes as a basis for the design of an actuation. The main question is whether applying such receptivity-based actuation during the period where instability would grow indeed alters the growth of the instability. With the application to the casting of alloys in mind, we would indeed seek to at least stifle, and possibly prevent the growth of the instability as much as possible. The mathematical expression of the corresponding actuation is provided by equation (19). Importantly, while the first three components of $\mathbf{f}(x, y, z, t)$ indeed represent a force density applied in the three components of the Navier–Stokes equation, the fourth component applies to the energy equation (2) and, therefore, represent a heat source. The full actuation, therefore, comprises both a momentum and an energy source in the general case.

4.1 Methodology

In the first instance, we seek the linear response of the system. This step acts as a validation, as the sensitivity analysis already provided us with an indication of the linear response we should expect. Two very important aspects still remain to be clarified by calculating the linear evolution of the leading eigenmode under the effect of the actuation: first, the timescale of the response and the duration of the effect are not considered in the receptivity analysis. Second, the receptivity does not specify how the relative amplitude and phase of the receptive mode affect the linear response. Indeed, in equation (19), the amplitude and phase of the actuation are both relative to the leading eigenmode. Since the receptivity mode is the solution of a homogeneous linear problem, none of them is specified. On the other hand the relative amplitude and phase of the actuation can be expected to greatly influence the system's response to it. For these two reasons, and to identify the combination of relative phase and amplitude that optimises the suppression of the instability, we run a series of linear simulations by adding a source term representing the receptivity-based actuation on the right-hand side of (9):

$$\frac{\partial \mathbf{q}'}{\partial t} = \mathcal{L} \mathbf{q}' + \mathbf{f}. \quad (20)$$

In our parametric study, we varied the phase ϕ from 0 to 2π in increments of $\pi/10$ and the amplitude between 0.01 and 0.5 for most of the cases. Each linear simulation is initiated using the unstable mode obtained from the LSA as the initial condition with amplitude such that

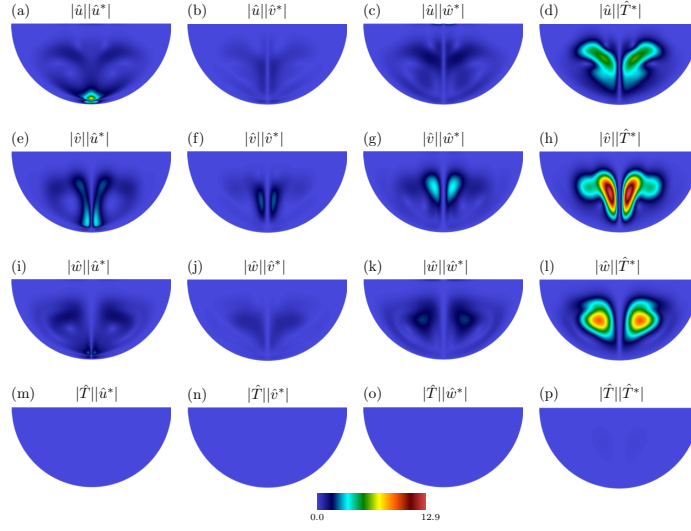


Figure 6: The absolute value of the components of the sensitivity tensor $S_{ij} = \hat{\mathbf{q}}_i \hat{\mathbf{q}}_j^*$ for the simulation case C3 ($Re = 100$, $Ra = 4 \times 10^4$, and $k = 4$) in the $x - y$ plane.

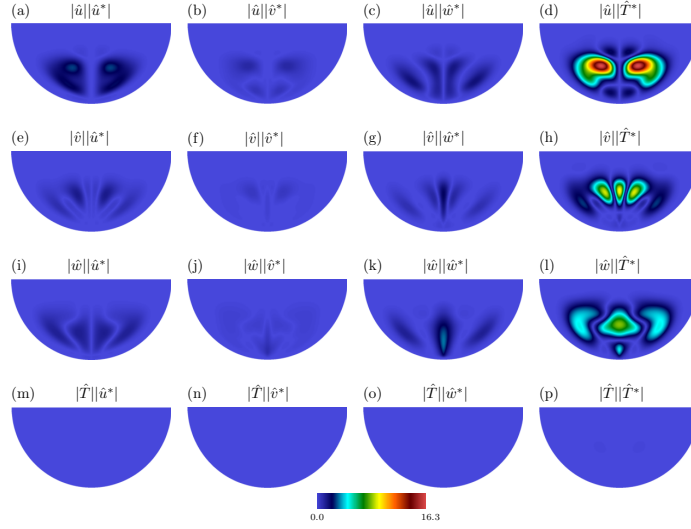


Figure 7: The absolute value of the components of the sensitivity tensor $S_{ij} = \hat{\mathbf{q}}_i \hat{\mathbf{q}}_j^*$ for the simulation case C4 ($Re = 150$, $Ra = 8 \times 10^4$, and $k = 6$) in the $x - y$ plane.

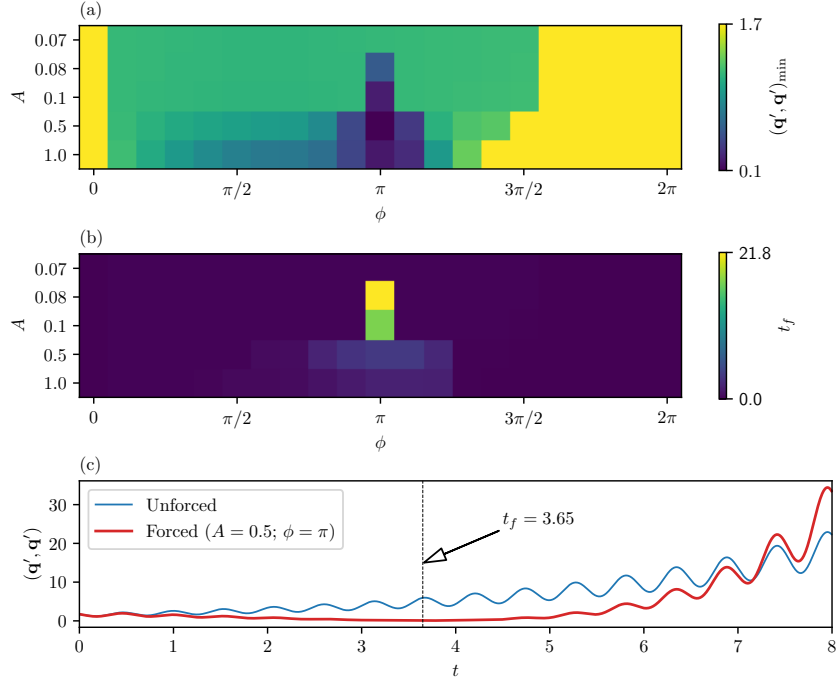


Figure 8: For the simulation case C1 ($Re = 0$, $Ra = 7 \times 10^3$, and $k = 6$): (a) Minimum value of the strength of perturbation $(\mathbf{q}', \mathbf{q}')_{\min}$ as a function of the amplitude A and the phase ϕ of the linear receptivity-based actuation. (b) Dependence of the time t_f at which $(\mathbf{q}', \mathbf{q}')_{\min}$ occurs on the amplitude A and phase ϕ . (c) The strength of perturbation $(\mathbf{q}', \mathbf{q}')$ as a function of time t for both unforced and forced cases.

the normalisation condition (18) is satisfied, from which both A and ϕ are fixed. In the linear simulation, normal modes are decoupled from each other so the time-dependent solution obtained by initialising the solution with a single normal mode reflects the evolution of that particular mode only. As such, linear simulations provide a direct measure of the ability of the actuation based on the receptivity mode to affect the evolution of the unstable mode. To quantitatively assess this effect, we monitor the time-dependent energy of the mode, $(\mathbf{q}', \mathbf{q}')$. The lowest value $(\mathbf{q}', \mathbf{q}')_{\min}$ reached by this quantity gives an indication of the damping achieved by the actuation, and the time of occurrence of this minimum measures the timescale over which this damping is achieved, denoted as t_f . Going back to the example of the continuous casting of alloys as one of the motivations for this work, the unstable mode may not need to be suppressed indefinitely. Instead, maintaining the unstable mode to a low level for the entire duration of the casting operation, which is finite, would be sufficient to ensure it does not impact the final quality of the alloy. Hence the importance of t_f is both fundamental and practical.

4.2 Analysis of cases C1-C4

We shall now examine the outcome of this approach in each of the C1-C4 cases, defined in § 2.4. Figure 8(c) illustrates two examples of the evolution of $(\mathbf{q}', \mathbf{q}')$ for C1. The blue curve represents a simulation with no actuation, *i.e.*, one with $A = 0$ amplitude. As predicted by LSA, the instability grows exponentially with oscillations of frequency determined by the imaginary part of the mode's eigenvalue. The red curve represents the case with receptivity-based actuation of amplitude $A = 0.5$ and phase $\phi = \pi$. In this case, $(\mathbf{q}', \mathbf{q}')$ decreases over time and reaches its minimum value at $t_f = 3.65$. For $t > t_f$, $(\mathbf{q}', \mathbf{q}')$ increases, and crosses the blue curve at $t = 7.16$. Hence, in this particular case, the actuation results in an effective suppression of the instability until $t = t_f$. Now, to determine the optimal value of A and ϕ , *i.e.*, values that achieve the smallest value of $(\mathbf{q}', \mathbf{q}')_{\min}$, we vary the phase in the range of 0 to 2π , and for amplitudes between 0.07 to 1.0. The grid map of the corresponding values of $(\mathbf{q}', \mathbf{q}')_{\min}$ is shown in figure 8(a) for C1. It turns out that $A = 0.5$ and $\phi = \pi$ are the optimal values of amplitude and phase with $(\mathbf{q}', \mathbf{q}')_{\min} = 0.06$.

Further calculations were performed for C2 and C3, which, despite corresponding to different instability branches, return similar results, presented in figures 9 and 10. As compared to C1, C2's optimal amplitude is twice as large, and its phase is shifted to the right. Therefore, the optimal values are $A = 1.0$ and $\phi = 1.7\pi$. The value of t_f is slightly reduced to 2.57. On the other hand, for C3, the optimal amplitude is reduced to 0.1, and the optimal phase is shifted to 1.5π . The value of t_f , however, is slightly increased to 3.93, which implies that the instability can be attenuated for a slightly longer period of time.

C4 differs from the other cases in that the leading eigenmode and its adjoint, which represents receptivity, are non-oscillatory. Consequently, the actuation is also non-oscillatory and we do not need to determine the optimal phase, only the optimal amplitude. In the

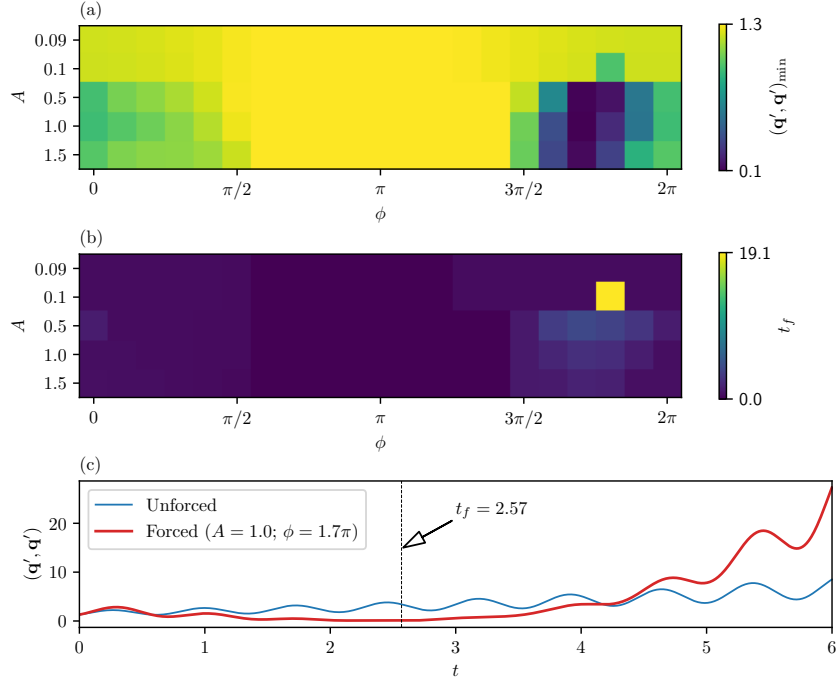


Figure 9: For the simulation case C2 ($Re = 50$, $Ra = 7 \times 10^3$, and $k = 6$): (a) Minimum value of the strength of perturbation $(\mathbf{q}', \mathbf{q}')_{\min}$ as a function of the amplitude A and the phase ϕ of the linear receptivity-based actuation. (b) Dependence of the time t_f at which $(\mathbf{q}', \mathbf{q}')_{\min}$ occurs on the amplitude A and phase ϕ . (c) The strength of perturbation $(\mathbf{q}', \mathbf{q}')$ as a function of time t for both unforced and forced cases.

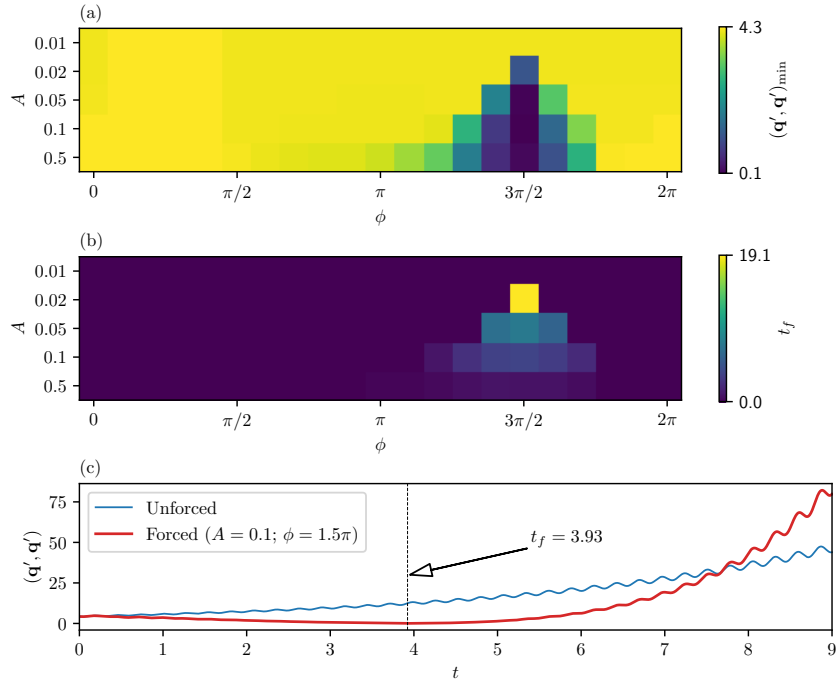


Figure 10: For the simulation case C3 ($Re = 100$, $Ra = 4 \times 10^4$, and $k = 4$): (a) Minimum value of the strength of perturbation $(\mathbf{q}', \mathbf{q}')_{\min}$ as a function of the amplitude A and the phase ϕ of the linear receptivity-based actuation. (b) Dependence of the time t_f at which $(\mathbf{q}', \mathbf{q}')_{\min}$ occurs on the amplitude A and phase ϕ . (c) The strength of perturbation $(\mathbf{q}', \mathbf{q}')$ as a function of time t for both unforced and forced cases.

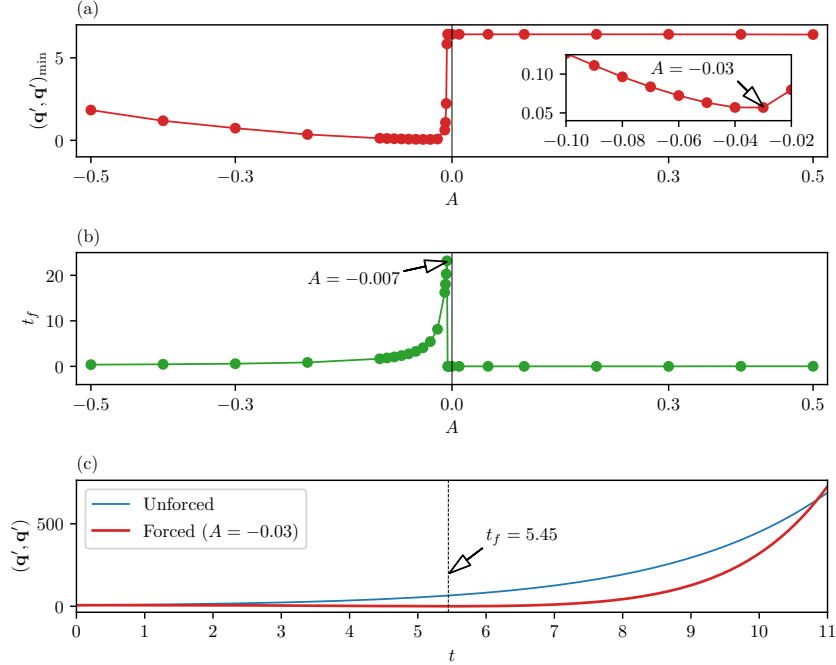


Figure 11: For the simulation case C4 ($Re = 150$, $Ra = 8 \times 10^4$, and $k = 6$):(a) Minimum value of the strength of perturbation $(\mathbf{q}', \mathbf{q}')_{\min}$ as a function of the amplitude A of the linear receptivity-based actuation. Inset represents the amplitude $A = -0.03$ which corresponds to the lowest value of $(\mathbf{q}', \mathbf{q}')_{\min}$. (b) Dependence of the time t_f at which $(\mathbf{q}', \mathbf{q}')_{\min}$ occurs on the amplitude A . (c) The strength of perturbation $(\mathbf{q}', \mathbf{q}')$ as a function of time t for both unforced and forced cases.

absence of a phase, the possibility still remains to reverse the actuation, which we incorporated into the sign of A . The variations of $(\mathbf{q}', \mathbf{q}')_{\min}$ with A are shown in figure 11(a). For $A \geq 0$, $(\mathbf{q}', \mathbf{q}')_{\min}$ remains very close to the initial value of $(\mathbf{q}', \mathbf{q}')$ so no suppression is achieved. For $A < 0$, by contrast, we observe a sudden drop in the value of $(\mathbf{q}', \mathbf{q}')_{\min}$ at very small amplitudes, with a minimum value at $A = -0.03$ (see inset of figure 11(a)).

Figure 11(c) shows the evolution of $(\mathbf{q}', \mathbf{q}')$ over time for both the unforced and forced cases with $A = -0.03$. It appears that the actuation achieves a suppression of the non-oscillatory mode up to time 5.45.

4.3 The salient features of the linear response

All four cases show strong similarities, despite the differences in the nature of the unstable modes. First, the linear actuation remains effective only for a finite time t_f . Beyond this point, the unstable mode grows again and at a faster pace than when unforced. This means that for $t > t_f$, the linear actuation becomes *destabilising*. Table 3 shows that t_f remains of the order of the inverse of the growthrate of the unstable mode, as the ratio σt_f remains of the order of unity for all suppression-optimising cases. The term ‘‘suppression-optimising’’ refers to seeking the amplitude and phase of the forcing that achieve the maximum reduction in mode amplitude. The reduction in mode

Simulation Case	Suppression-optimising		Time-optimising	
	σt_f	$\frac{(\mathbf{q}', \mathbf{q}')_{\min}}{(\mathbf{q}', \mathbf{q}')_{t=0}}$	σt_f	$\frac{(\mathbf{q}', \mathbf{q}')_{\min}}{(\mathbf{q}', \mathbf{q}')_{t=0}}$
C1	0.57	0.037	3.43	0.314
C2	0.31	0.040	2.34	0.733
C3	0.51	0.013	2.51	0.272
C4	1.16	0.009	4.93	0.910

Table 3: The normalised value of t_f with respect to the growth rate σ for various suppression-optimising and time-optimising simulation cases. Comparison of $(\mathbf{q}', \mathbf{q}')_{\min}$ relative to the initial value of $(\mathbf{q}', \mathbf{q}')$ is shown for each suppression-optimising and time-optimising simulation cases.

Case	Re	Ra	N	Δt	\mathcal{R}_A	t_f	t_{eff}	$\frac{t_{\text{eff}}}{t_f}$	η_a
C1	0	7×10^3	6	5×10^{-3}	1×10^{-2}	3.65	19.1	5.23	5.21
C2	50	7×10^3	7	1×10^{-4}	4×10^{-4}	2.57	17.8	6.93	6.30
C3	100	4×10^4	7	1×10^{-4}	1×10^{-3}	3.92	32.5	8.29	8.27
C4	150	8×10^4	8	5×10^{-5}	4×10^{-5}	5.45	21.4	3.93	3.93

Table 4: Parameters of our numerical calculations: Reynolds number Re , Rayleigh number Ra , order of polynomial N , time step Δt . Amplitude ratio \mathcal{R}_A , the forcing cut-off time t_f , nonlinear efficiency time $t_{\text{eff}} = t_2 - t_1$, and actuation efficiency $\eta_a = t_R/t_f$ based on recovery time t_R such that $(\mathbf{q}', \mathbf{q}')_{t=t_R} = (\mathbf{q}', \mathbf{q}')_{t=0}$ for the 3D DNS.

amplitude achieved at $t = t_f$ is of approximately two orders of magnitudes (see table 3) for the suppression-optimising cases. This suggests that the actuation is more effective when applied for a finite time t_f , then stopped until the unstable mode regrows to its initial amplitude (*i.e.* during a time $\sim \sigma^{-1}$), at which point the procedure can be repeated. Whether this strategy is realistic depends on how this pattern is affected by nonlinearities.

This pattern also raises the question whether instead of applying suppression-optimising, it may be beneficial to seek configurations that achieve the largest value of t_f so as to maximise the time during which the suppression is effective. The term “time-optimising” is introduced to denote the search for amplitude and phase settings that maximise the value of t_f . The corresponding optimal values are shown on figures 8(b), 9(b), 10(b), and 11(b). Unsurprisingly, actuation parameters optimising the suppression and t_f differ. We shall compare how both optimals perform on the nonlinear response in the next section.

5 Nonlinear response to an actuation based on receptivity

5.1 Methodology

The linear simulations confirmed that an actuation designed from the topology of the receptivity, with a frequency matched to the leading eigenmode was indeed capable of stifling the linear mechanism responsible for the growth of the leading eigenmode. We also identified the relative amplitude and phase that maximised its suppression. In reality, the finite amplitude of the perturbation, whether subject to the actuation or not, activates a nonlinear response of the system. Although nonlinearities may not measurably deflect the perturbation’s evolution in its early stages, when its amplitude is still small, it is likely to govern its dynamics at longer timescales, especially at the point where the actuation ceases to be efficient. For this reason, the nonlinear effects are essential to determine how effective the actuation may be at suppressing instabilities, and how long it may remain so.

Including the nonlinear dynamics, however, raises several technical difficulties. First, the optimal amplitude and phase were determined without any consideration of nonlinearity, so we may question whether these remain optimal for the nonlinear evolution. The answer lies partly in how the suppression is assessed. Following the approach we adopted in the linear study, we sought the point of lowest amplitude for the leading eigenmode and the time of this minimum. Since the evolution from an infinitesimal perturbation to that point involves only very small amplitudes, it is legitimate to assume that nonlinearities would play little role there and that, consequently, the linear and the nonlinear evolutions would remain very similar during this phase [17]. One should, however, keep in mind that if phase and amplitude were sought so as to optimise the saturated state of the evolution, the full nonlinear equations would need to be included in the optimisation process [48]. However, our specific purpose of understanding the influence of the nonlinear effects is better served by keeping a similar approach to the linear study. Additionally, since the linear study showed that the growth of the leading eigenmode was only effectively suppressed until $t = t_f$, we shall only apply the actuation up to that time, and let the flow evolve freely after that time.

Second, the definition of the initial conditions for the nonlinear problem differs from the linear one: the linear equations indeed return the same evolution regardless of the amplitude of the initial condition (up to a multiplicative factor), and only the relative amplitude and phase of the actuation mattered. To transpose our approach into the nonlinear framework, we shall also specify the amplitude and phase of the actuation relative to the perturbation. In the nonlinear equations, however, if the unstable mode is left to grow “naturally” from noise, its amplitude and phase are not specified in the initial condition, so actuation cannot be fixed *a priori*. A workaround would be to let the unstable mode develop up to a trigger-amplitude, where both amplitude and phase can be measured, and then apply the optimal actuation based on these. Indeed, such an approach would be required in a real process where the onset of instability would need to be detected for the actuation to be activated. For instance, electromagnetic sensors [14, 56] can detect the onset of such instabilities. Since our previous study of the free nonlinear evolution of the leading eigenmode confirmed that it emerged naturally from noise [28], we shall directly initiate the nonlinear simulation with the leading eigenmode set to an amplitude such its ratio to the base flow

$$\mathcal{R}_A = \frac{(\mathbf{q}', \mathbf{q}')}{(\mathbf{Q}, \mathbf{Q})} \quad (21)$$

remained much smaller than unity (see table 4). Here, $\mathbf{Q} = (\mathbf{U}, T)^\top$ represents the steady base flow. Note that for the nonlinear simulations, \mathbf{q}' is obtained by subtracting the base flow from the entire flow field.

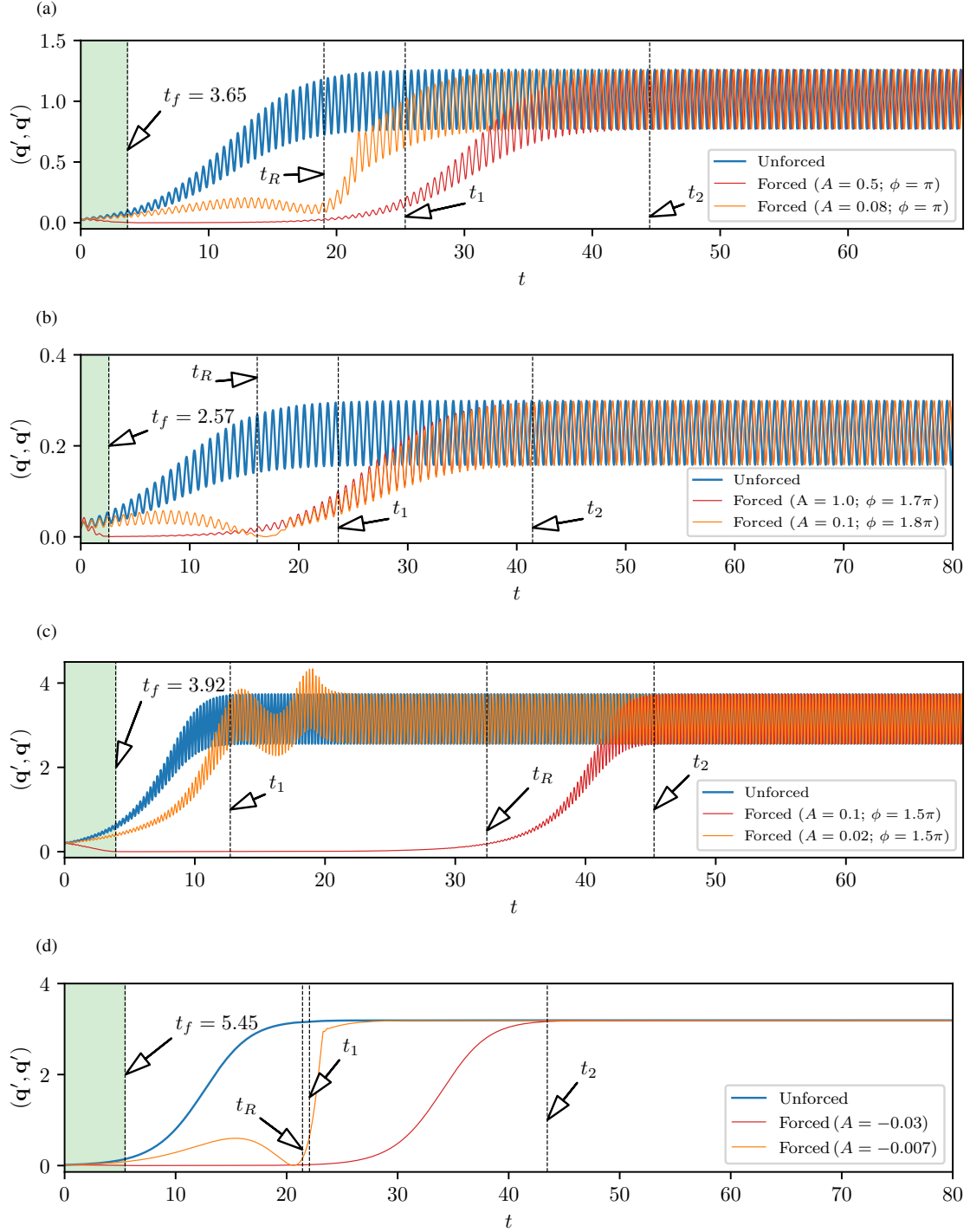


Figure 12: As a function of time t , the nonlinear evolution of the perturbation energy (q', q') , in the simulation cases (a) C1, (b) C2, (c) C3, and (d) C4, without actuation (blue), with actuation maximising t_f (orange) and with actuation achieving maximum reduction of energy (red).

5.2 Analysis of cases C1-C4

The evolution of the perturbation with and without actuation for case C1 is shown in figure 12(a). The blue curve illustrates the free nonlinear evolution with the flow initialised with the leading eigenmode for case C1 and no actuation applied. Initially, the energy of the perturbation (q' , q') grows exponentially, as predicted by the linear theory, and this confirms that nonlinear effects do not affect the early stages. These indeed induce a saturation at $t = t_1 = 25.4$. The envelope of the curve provides an estimate of the saturation time, denoted as t_1 . We consider the saturation time to be reached when the derivative of the envelope with respect to time falls below 10^{-3} . The red curve represents the evolution of the perturbation for the same initial conditions, but this time, with the suppression-optimising actuation applied as we just described. Until $t \approx 10$, the actuation results in a decrease of the perturbation's amplitude, after which the perturbation begins to grow slowly. Interestingly, the decay of the perturbation continues well beyond the time of minimum amplitude found in the linear simulation. Since, however, nonlinear effects are not expected to play a role for such low amplitudes, as suggested by the exponential form of the actuation-free evolution, the difference more likely results from switching off the actuation at t_f in the nonlinear simulations. Given the very low amplitude of the perturbation around $t = t_f$, the system remains governed by linear dynamics so the reason for the extended period of suppression is that exponential growth from such a low level of perturbation simply extends over a longer period of time. This suggests that applying the actuation beyond the time of maximum growth suppression in fact promotes the growth of the eigenmode. As such, switching off the actuation at t_f is optimal. The underlying suppression strategy, is then to suppress the leading eigenmode down to the lowest possible amplitude so that the linear mechanism takes as long as possible to act. The nonlinear dynamics only provide a measure of when this strategy ceases to be effective.

Indeed, after $t \approx 20$, the exponential growth becomes sufficient to activate nonlinearities and the perturbation amplitude reaches nonlinear saturation at $t = t_2$ (t_2 is calculated using the same method as t_1 by analysing the envelope of the curve). In order to estimate the effectiveness of the actuation at suppressing the instability, we define the nonlinear efficiency time, $t_{\text{eff}} = t_2 - t_1$, which for C1 is $19.1 \simeq 5.23t_f$. In other words, the actuation prevents nonlinear saturation during 5.23 times the duration of its application, *i.e.* it approximately doubles the time to saturation. Even more interestingly, the unstable mode returns to its initial amplitude at a time t_R , $\eta_a = 5.21$ times longer than t_f , so that it could potentially be indefinitely maintained at that level by applying the actuation during t_f every $\eta_a t_f$, which costs η_a less energy than applying the actuation continuously. These results are very encouraging since they validate of the linear approach, and show that the receptivity forcing obtained from the linear analysis is indeed capable of suppressing the growth of the instability in the full nonlinear system for a long time, not only compared to the timescale of growth of the instability and to the duration of the actuation t_f .

In addition to applying actuation based on the minimum value of (q', q') , we also tested the actuation strategy based on the forcing maximising t_f . For Case C1, the highest t_f value of 19.1 is achieved for $A = 0.08$ and $\phi = \pi$. The simulation corresponding to these parameters is depicted by the orange curve in figure 12(a). Interestingly, the perturbation energy remains below that of the unforced case until around $t \approx 20$, yet it consistently stays higher than that of the mode with suppression-optimising actuation ($A = 0.5$), before reaching nonlinear saturation. Since the perturbation energy for $A = 0.08, \phi = \pi$ exceeds that of $A = 0.5, \phi = \pi$, its nonlinear saturation occurs prior to the case of $A = 0.5$. This means that suppression-optimising actuation outperforms time-optimising actuation.

Case C2 returned exactly the same phenomenology for the suppression-optimising actuation, despite the difference in the nature of the leading eigenmodes (see figure 12(b)). The values of t_{eff}/t_f and η_a are not significantly different than for C1, but the time-optimising actuation incurs a different behaviour: although the unstable mode does not initially decay, it decays briefly at a much later time than for the actuation optimising suppression, down to a similar level. Shortly after, however, both curves practically coincide and simultaneously evolve to saturation. In this sense both actuations perform equally well: This is the only case where the suppression-optimising actuation does not significantly outperform the time-optimising actuation. Nevertheless, since the perturbation remains at a much lower level in the initial stages of evolution for the latter, it is still overall better at suppressing the unstable mode.

Case C3 also produced the same phenomenology shown on figure 12(c), but with increased values of $t_{\text{eff}}/t_f = 8.29$ and $\eta_a = 8.27$, *i.e.* with a much higher efficiency of the suppression-optimising actuation. By contrast with C2, however, the time-optimising actuation is practically ineffective at suppressing the unstable mode as its amplitude grows to saturation barely later than without any actuation.

Lastly, we applied constant actuations in the nonlinear simulation of case C4, since the unstable mode is non-oscillatory. Once again, we used the unstable mode as the initial condition. The non-oscillatory nature of the mode does not seem to play a role as the evolution of the mode's energy in all three simulations, without actuation, with suppression-optimised actuation and with time-optimising actuation show very similar features to C1 and C3, with $t_{\text{eff}}/t_f \approx \eta_a = 3.93$.

5.3 The salient features of the nonlinear evolution

The overall outcome of the nonlinear simulations is that the phenomenology seen on in the linear simulation remains valid until the nonlinear effects become important and crucially, this happens when the saturation starts. If an actuation based on the adjoint mode, applied up to the time of maximum suppression t_f the unstable mode does not regain its initial amplitude until a time $\eta_a t_f$, roughly an order of magnitude longer than t_f ($\eta_a = 8.27$ in the most favourable case C3), so as long as the amplitude and phase of the actuation are optimised for suppression (and not for t_f). Until that point, the evolution follows mostly the linear dynamics, as the energy of the unstable mode remains small compared to that of the base flow. The nonlinear effects act shortly after this time, and when they do so, they incur growth up to the same point of saturation as when no actuation is applied. Hence, the strategy of repeating a sequence where the suppression-optimising actuation is applied until t_f , then switched off to let the flow evolve until $\eta_a t_f$, may indefinitely keep the

flow evolution in the linear regime, for which the actuation remains effective. Thus, this strategy may confine oscillations to very small amplitudes for an arbitrary length of time.

6 Conclusions

Inspired by the process of continuous casting of liquid metal alloy, we sought to model the suppression of oscillations in mixed baroclinic convection in a nearly hemispherical cavity. This problem offered us an opportunity to assess the feasibility of suppressing oscillatory instabilities by means of an actuation modelled on the receptivity map of unstable modes. Doing so led us to consider four canonical cases spanning the three branches of instability for this problem [28]: a purely convective flow subject to a supercritical oscillatory instability (C1), a mixed convective flow subject to a supercritical oscillatory instability (C2), a mixed convective flow subject to a subcritical oscillatory instability (C3), and a mixed convective flow subject to a supercritical non-oscillatory instability (C4).

For this, we first identified the receptivity map for each of these cases. We found that as the intensity of the inflow increases, the region of receptivity becomes increasingly concentrated near the inlet surface, *i.e.* increasingly favourable in the industrial context where immersing an actuator in the bulk of the melt over extended periods of time is not a feasible option. Analysis of the sensitivity tensor then showed that for the low Prandtl number of liquid metals, the temperature does not respond to any actuation, whether thermal or mechanical, whereas the velocity field is responsive to both thermal and mechanical actuation. This is understandable since thermal diffusion acts nearly two orders of magnitudes faster than viscous diffusion. As such, acting on the temperature field would require an actuation $\mathcal{O}(Pr)$ faster than one acting on the velocity field. For C2-C4, the sensitivity analysis then predicted that the area where the instability grows would be significantly affected by an actuation located in the receptive region. This was not the case for C1, which questioned whether such an actuation would be effective in this case. With these results in hand, we performed linear and nonlinear simulations of the evolution of the unstable mode with and without actuation to answer the four questions set out in the introduction:

- (i) Since, for all cases (except C1), the area of receptivity is located near the inflow surface, the most efficient way to act on the instability in practice is to modify the inflow. In practice, this area is one of the most accessible in casting devices, so this result is favourable to the application. It must, nevertheless, be understood in the context of the simplified model we are considering here, and the question remains open regarding how the receptivity area would change in a more realistic geometry.
- (ii) Implementing a thermo-mechanical actuation modelled on the topology of the adjoint to the unstable mode to be suppressed (*i.e.*, its receptivity map) led to a suppression of the unstable eigenmode. To find this result, we scanned possible values of the amplitude and phase of the actuation with respect to the unstable mode. In doing so, we found that it was always possible to find a combination of amplitude and phase of the actuation leading to a significant suppression of the unstable mode. Typically, its energy could be reduced by two orders of magnitude, even in case C1, where the sensitivity map did not coincide very well with the location of the instability.
- (iii) The actuation only had a stabilising effect during a finite time t_f of the order of the inverse growth rate of the unstable mode σ^{-1} , after which linear simulations proved it to be *destabilising*, in the sense that it enhances the growth of the unstable mode, compared to the simulations without actuation. This led us to consider two strategies for the design of the actuation: one where amplitude and phase of the actuation are chosen to optimise the suppression of the mode's energy (suppression-optimising actuation), and one optimising t_f , *i.e.* for which the decay of the unstable mode is the longest (time-optimising actuation).
- (iv) For this reason, to evaluate the influence of nonlinearities, we calculated the evolution of the unstable mode through the full nonlinear governing equations, with either type of actuation applied during t_f , after which the flow was left to evolve freely. With suppression-optimising actuation, the energy of the unstable mode always decayed well beyond t_f before it slowly re-grew, to recover its initial amplitude at a time $\eta_a t_f$ typically an order of magnitude greater than t_f . In that sense η_a measures the efficiency of the actuation. Time-optimised actuation always led to significantly lower values of η_a , and even to no suppression at all in case C3. Shortly after $\eta_a t_f$, nonlinearities incurred a rapid growth leading to a saturation at the same level as nonlinear simulations without actuation.

Crucially, these results applied to all four cases, regardless of whether the unstable mode is oscillatory or not, and whether it arises through a supercritical or a subcritical bifurcation. These results open interesting perspectives in view of the suppression of the instability. A possible strategy would consist in applying a mechanical actuation in the inflow region based on the receptivity map of the unstable mode, with amplitude and phase chosen to optimise the suppression of the optimal mode, through the *linear* evolution equations. Actuation should then be applied from the point where the unstable mode reaches a small, arbitrary threshold amplitude, until time t_f . For $t > t_f$, the flow should be left to evolve until the unstable mode regains its initial threshold amplitude, at $t = \eta_a t_f$, at which point the actuation should be applied again, iterating the procedure for as long as the flow needs to be stabilised. The success of this strategy relies on the assumption that the threshold amplitude is sufficiently small for the unstable mode to evolve according to the linear equations. In other words, the strategy consists of preventing it from entering a nonlinear regime where the actuation would become ineffective.

The application of this idea raises a number of questions for further studies. First, we considered only a single unstable mode (or at most two), which restricts the approach to weak supercriticalities only. In more supercritical flows, several modes may become unstable. Since, however, the approach is linear, a linear combination of optimal actuations for each of the unstable mode may succeed in stabilising all of them, provided transient growth due to their possible non-orthogonality does not lead to perturbation amplitudes capable of igniting

nonlinearities [52]. Such an approach may involve the stabilisation of modes from different branches if the flow becomes multi-modal, as for example magnetoconvective flows do [61]. In case one of these modes is subcritical (as for case C3), there is an additional risk that an altogether different branch of instability may drive the transition, even below the critical Rayleigh number of the linear stability of the leading eigenmode.

Acknowledgements

Our numerical simulations were performed on *Zeus* of Coventry University and the *Sulis* Tier 2 HPC platform hosted by the Scientific Computing Research Technology Platform at the University of Warwick. A. Poth erat acknowledges support from the Royal Society under the Wolfson Research Merit Award Scheme (grant reference WM140032).

References

- [1] J. G. Aguilar and M. P. Juniper. Thermoacoustic stabilization of a longitudinal combustor using adjoint methods. *Phys. Rev. Fluids*, 5:083902, 2020.
- [2] A. V. Anilkumar, R. N. Grugel, X. F. Shen, C. P. Lee, and T. G. Wang. Control of thermocapillary convection in a liquid bridge by vibration. *J. Appl. Phys.*, 73(9):4165–4170, 05 1993.
- [3] K. Aujogue, A. Poth erat, and B. Sreenivasan. Onset of plane layer magnetoconvection at low Ekman number. *Phys. Fluids*, 27(10):106602, 2015.
- [4] D. Barkley, H. M. Blackburn, and S. J. Sherwin. Direct optimal growth analysis for timesteppers. *Intl J. Numer. Meth. Fluids*, 57(9):1435–1458, July 2008.
- [5] H. H. Bau. Control of Marangoni–B enard convection. *Int. J. Heat Mass Transfer*, 42:1327–1341, 1999.
- [6] C. Beckermann. Macrosegregation. In K. Buschow, R. W. Cahn, M. C. Flemings, B. Ilchner, E. J. Kramer, S. Mahajan, and P. Veyssi ere, editors, *Encyclopedia of Materials: Science and Technology*, pages 4733–4738. Elsevier, Oxford, 2001.
- [7] A. Bolis, C. D. Cantwell, D. Moxey, D. Serson, and S. J. Sherwin. An adaptable parallel algorithm for the direct numerical simulation of incompressible turbulent flows using a Fourier spectral/hp element method and MPI virtual topologies. *Comput. Phys. Comm.*, 206:17–25, Sept. 2016.
- [8] J. Boussinesq. *Theorie Analytique de la Chaleur*, volume 2. Gauthier-Villars, Paris, 1903.
- [9] L. Brandt, O. Marquet, J. O. Pralits, and D. Sipp. Effect of base-flow variation in noise amplifiers: the flat-plate boundary layer. *J. Fluid Mech.*, 687:503–528, 2011.
- [10] H.-P. Bunge, C. R. Hagelberg, and B. J. Travis. Mantle circulation models with variational data assimilation: inferring past mantle flow and structure from plate motion histories and seismic tomography. *Geophys. J. Int.*, 152(2):280–301, 02 2003.
- [11] C. D. Cantwell, D. Moxey, A. Comerford, A. Bolis, G. Rocco, G. Mengaldo, D. D. Grazia, S. Yakovlev, J. E. Lombard, D. Ekelschot, B. Jordi, H. Xu, Y. Mohamied, C. Eskilsson, B. Nelson, P. Vos, C. Biotto, R. M. Kirby, and S. J. Sherwin. Nektar++: An open-source spectral/hp element framework. *Comput. Phys. Comm.*, 192:205–219, July 2015.
- [12] S. Chandrasekhar. *Hydrodynamic and Hydromagnetic Stability*. Clarendon Press, 1961.
- [13] K. K. Chen and G. R. Spedding. Boussinesq global modes and stability sensitivity, with applications to stratified wakes. *J. Fluid Mech.*, 812:1146–1188, Jan. 2017.
- [14] S.-M. Cho and B. G. Thomas. Electromagnetic forces in continuous casting of steel slabs. *Metals*, 9:471, 2019.
- [15] R. Dorward, D. Beerntsen, and K. Brwon. Banded segregation patterns in DC-cast Al-Zn-Mg-Cu alloy ingots and their effect on plate properties. *Aluminium*, 72(4):251–259, 1996.
- [16] A. P. Dowling and A. S. Morgans. Feedback control of combustion oscillations. *Ann. Rev. Fluid Mech.*, 37(1):151–182, 2005.
- [17] P. G. Drazin and W. H. Reid. *Hydrodynamic Stability*. Cambridge Mathematical Library. Cambridge University Press, 2 edition, 2004.
- [18] I. A. Eltayeb. Hydromagnetic convection in a rapidly rotating fluid layer. *Proc. R. Soc. A*, 326(1565):229–254, 1972.
- [19] S. C. Flood and P. A. Davidson. Natural convection in aluminium direct chill cast ingot. *Materials Science and Technology*, 10(8):741–752, 1994.
- [20] C. Geuzaine and J.-F. Remacle. Gmsh Reference Manual. Gmsh: A Three-Dimensional Finite Element Mesh Generator With Built-in Pre-and Post-Processing Facilities. *Int. J. Numer. Methods Eng.*, 79(1309), 2009.
- [21] F. Giannetti, S. Camarri, and P. Luchini. Structural sensitivity of the secondary instability in the wake of a circular cylinder. *J. Fluid Mech.*, 651:319 – 337, 03 2010.

- [22] F. Giannetti and P. Luchini. Structural sensitivity of the first instability of the cylinder wake. *J. Fluid Mech.*, 581:167–31, May 2007.
- [23] A. Horbach, B. H.-P., and J. Oeser. The adjoint method in geodynamics: derivation from a general operator formulation and application to the initial condition problem in a high resolution mantle circulation model. *Int. J. Geomath*, 5:163–194, 2014.
- [24] S. Horn and J. M. Aurnou. The Elbert range of magnetostrophic convection. I. linear theory. *Proc. R. Soc. A.*, 478:20220313, 2022.
- [25] S. Horn and J. M. Aurnou. The Elbert range of magnetostrophic convection. II: comparing linear predictions to nonlinear DNS. *Under consideration for publication in Proc. Roy. Soc. A*, 2023.
- [26] A. Ismail-Zadeh, G. Schubert, I. Tsepelev, and A. Korotkii. Inverse problem of thermal convection: numerical approach and application to mantle plume restoration. *Phys. Earth Planet. Inter.*, 145(1):99–114, 2004.
- [27] M. P. Juniper and R. I. Sujith. Sensitivity and nonlinearity of thermoacoustic oscillations. *Ann. Rev. Fluid Mech.*, 50(1):661–689, 2018.
- [28] A. Kumar and A. Poth erat. Mixed baroclinic convection in a cavity. *J. Fluid Mech.*, 885:5885–31, Feb. 2020.
- [29] P. V. Kungurtsev and M. P. Juniper. Adjoint based shape optimization of the microchannels in an inkjet printhead. *J. Fluid Mech.*, 871:113–138, 2019.
- [30] A. V. Kuznetsov. Double-diffusive convection during continuous strip casting. *CHT’97 - Advances in Computational Heat Transfer. Proceedings of the International Symposium -  esme, Turkey, May 26 - 30, 1997*, 1997.
- [31] T. C. Lieuwen. Combustion driven oscillations in gas turbines. In *Turbomachinery International*, pages 16–18. Turbomachinery International Publications., 2003.
- [32] E. Lubarsky, D. Shcherbik, A. Bibik, and B. T. Zinn. Active control of combustion oscillations by non-coherent fuel flow modulation. In *9th AIAA/CEAS Aeroacoustics Conference and Exhibit*, page 3180, 2003.
- [33] P. Luchini and A. Bottaro. Adjoint equations in stability analysis. *Ann. Rev. Fluid Mech.*, 46:493–517, 2014.
- [34] L. Magri and M. P. Juniper. Sensitivity analysis of a time-delayed thermoacoustic system via an adjoint-based approach. *J. Fluid Mech.*, 719:183–202, 2013.
- [35] L. Magri and M. P. Juniper. Global modes, receptivity, and sensitivity analysis of diffusion flames coupled with duct acoustics. *J. Fluid Mech.*, 752:237–265, 2014.
- [36] X. Mao, H. M. Blackburn, and S. J. Sherwin. Nonlinear optimal suppression of vortex shedding from a circular cylinder. *J. Fluid Mech.*, 775:241–265, June 2015.
- [37] O. Marquet, D. Sipp, and L. Jacquin. Sensitivity analysis and passive control of cylinder flow. *J. Fluid Mech.*, 615:221–252, 2008.
- [38] K. McManus, U. Vandsburger, and C. Bowman. Combustor performance enhancement through direct shear layer excitation. *Combust. Flame*, 82(1):75–92, 1990.
- [39] A. Medelfef, D. Henry, S. Kaddeche, F. Mokhtari, S. Bouarab, V. Botton, and A. Bouabdallah. Linear stability of natural convection in a differentially heated shallow cavity submitted to high-frequency horizontal vibrations. *Phys. Fluids*, 35(8):084107, 08 2023.
- [40] K. Momose, K. Sasoh, and H. Kimoto. Thermal boundary condition effects on forced convection heat transfer. *JSME International Journal Series B Fluids and Thermal Engineering*, 42(2):293–299, 1999.
- [41] H. C. Mongia, T. J. Held, G. C. Hsiao, and R. P. Pandalai. Challenges and progress in controlling dynamics in gas turbine combustors. *J. Prop. Power*, 19(5):822–829, 2003.
- [42] D. Moxey, C. D. Cantwell, Y. Bao, A. Cassinelli, G. Castiglioni, S. Chun, E. Juda, E. Kazemi, K. Lackhove, J. Marcon, G. Mengaldo, D. Serson, M. Turner, H. Xu, J. Peir o, R. M. Kirby, and S. J. Sherwin. Nektar++: Enhancing the capability and application of high-fidelity spectral/hp element methods. *Comput. Phys. Comm.*, 249:107110, Apr. 2020.
- [43] Y. Nakagawa. Experiments on the instability of a layer of mercury heated from below and subject to the simultaneous action of a magnetic field and rotation. *Proc. R. Soc. A*, 242(1228):81–88, 1957.
- [44] N. Noiray, D. Durox, T. Schuller, and S. Candel. Dynamic phase converter for passive control of combustion instabilities. *Proc. Combust. Inst.*, 32(2):3163–3170, 2009.
- [45] A. Oberbeck.  ber die W rmeleitung der Fl ussigkeiten bei Ber cksichtigung der Str mungen infolge von Temperaturdifferenzen. *Ann. Phys. Chem.*, 243(6):271–292, 1879.
- [46] J. Park and T. A. Zaki. Sensitivity of high-speed boundary-layer stability to base-flow distortion. *J. Fluid Mech.*, 859:476–515, 2019.
- [47] R. T. Pierrehumbert and K. L. Swanson. Baroclinic instability. *Ann. Rev. Fluid Mech.*, 27(1):419–467, 1995.
- [48] C. C. T. Pringle, A. P. Willis, and R. R. Kerswell. Minimal seeds for shear flow turbulence: using nonlinear transient growth to touch the edge of chaos. *J. Fluid Mech.*, 702:415–443, May 2012.

- [49] U. A. Qadri, D. Mistry, and M. P. Juniper. Structural sensitivity of spiral vortex breakdown. *J. Fluid Mech.*, 720:558–581, Feb. 2013.
- [50] P. H. Roberts and E. M. King. On the genesis of the Earth’s magnetism. *Rep. Prog. Phys.*, 76:096801, sep 2013.
- [51] H. Salwen and C. E. Grosch. The continuous spectrum of the Orr-Sommerfeld equation. Part 2. Eigenfunction expansions. *J. Fluid Mech.*, 104:445–465, 1981.
- [52] P. J. Schmid and D. S. Henningson. *Stability and Transition in Shear Flows*. Springer-Verlag New York, 2001.
- [53] D. Sheng and L. Jonsson. Two-fluid simulation on the mixed convection flow pattern in a nonisothermal water model of continuous casting tundish. *Metall. Mater. Trans. B*, 31(4):867–875, 2000.
- [54] P. J. Strykowski and K. R. Sreenivasan. On the formation and suppression of vortex ‘shedding’ at low Reynolds numbers. *J. Fluid Mech.*, 218:71–107, 1990.
- [55] J. Tang and H. H. Bau. Numerical investigation of the stabilization of the no-motion state of a fluid layer heated from below and cooled from above. *Phys. Fluids*, 10:1597–1610, 1998.
- [56] B. G. Thomas, Q. Yuan, S. Sivaramakrishnan, T. Shi, S. P. Vanka, and M. B. Assar. Comparison of four methods to evaluate fluid velocities in a continuous slab casting mold. *ISIJ International*, 41(10):1262–1271, 2001.
- [57] B. G. Thomas and L. Zhang. Mathematical modeling of fluid flow in continuous casting. *ISIJ International*, 41(10):1181–1193, 2001.
- [58] D. J. Tritton. *Physical Fluid Dynamics*. Clarendon Press, Oxford, 1988.
- [59] T. Vo, A. Pothérat, and G. J. Sheard. Linear stability of horizontal, laminar fully developed, quasi-two-dimensional liquid metal duct flow under a transverse magnetic field and heated from below. *Phys. Rev. Fluids*, 2(3):033902, 2017.
- [60] P. E. J. Vos, C. Eskilsson, A. Bolis, S. Chun, R. M. Kirby, and S. J. Sherwin. A generic framework for time-stepping partial differential equations (PDEs): general linear methods, object-oriented implementation and application to fluid problems. *Intl. J. Comput. Fluid Dyn.*, 25(3):107–125, Mar. 2011.
- [61] Y. Xu, S. Horn, and J. M. Aurnou. Transition from wall modes to multimodality in liquid gallium magnetoconvection. *Phys. Rev. Fluids*, 8:103503, 2023.